

Full paper

Lead-free monocrystalline perovskite resistive switching device for temporal information processing

Jing-Yu Mao^a, Zhi Zheng^b, Zi-Yu Xiong^c, Pu Huang^c, Guang-Long Ding^a, Ruopeng Wang^{d,e}, Zhan-Peng Wang^a, Jia-Qin Yang^{d,e}, Ye Zhou^a, Tianyou Zhai^{b,**}, Su-Ting Han^{e,*}

^a Institute for Advanced Study, Shenzhen University, Shenzhen, 518060, PR China

^b State Key Laboratory of Material Processing and Die & Mould Technology, School of Materials Science and Engineering, Huazhong University of Science and Technology (HUST), Wuhan, 30074, PR China

^c College of Physics and Optoelectronics, Shenzhen University, Shenzhen, 518060, PR China

^d College of Electronics and Information Engineering, Shenzhen University, Shenzhen, 518060, PR China

^e Institute of Micro Optoelectronics, Shenzhen University, Shenzhen, 518060, PR China

ARTICLE INFO

Keywords:

Lead-free perovskite
Resistive switching
Ionic dynamics
Temporal information processing
Reservoir computing

ABSTRACT

Lead-free halide perovskites are emerging as promising candidate for practical application of optoelectronic devices due to their nontoxicity. Unfortunately, previously-reported lead-free halide perovskites-based resistive switching devices suffer from high leakage and operating current stemmed from the intrinsic nature of polycrystalline film with a great amount of grain boundaries and pin-holes. Here, we report for the first time a monocrystalline lead-free Cs₃Sb₂Br₉ perovskite nanoflake based lateral-structured device capable of combining nonvolatile bipolar switching and threshold switching with record-low switching electric field of 2.2×10^5 V m⁻¹. Confirmed by elemental analysis and theoretical calculation, migration of highly mobile Br vacancy with low activation energy in defects-free monocrystalline Cs₃Sb₂Br₉ is believed to be responsible for resistive switching. Short-term Ca²⁺ dynamics of biological synapses were then imitated by Cs₃Sb₂Br₉ resistive switching devices which were further implemented as an effective reservoir element. The construction of neural network-based reservoir computing system to efficiently process temporal information can be realized since its conductance states are determined by the history of external simulation.

1. Introduction

In the past few years, lead halide perovskites have become prevalent in the field of photovoltaic devices with ultra-high power conversion efficiency due to their outstanding optoelectronic property such as high optical absorption coefficient, long carrier life time, long diffusion length and adjustable bandgap [1,2]. Resistive switching (RS) devices based on lead halide perovskites have also drawn great attention owing to the feasibility of low-cost solution process and excellent RS behavior arising from their intrinsic ionic migration characteristics [3–12]. However, the lead containing perovskite is toxic and not environment-friendly, which pose critical challenges for potential commercialization in view of environmental issues [13,14]. Moreover, the organic-inorganic hybrid lead halide perovskite suffers from

instability against heat and moisture, let alone device degradation during measurement with eclipse of time. Taking on this perspective, more attentions should be focused on the substitution of Pb ion with other nontoxic isoelectronic metal cations with low toxicity to alleviate the impact on the environment, in addition to the efforts in enhancing the optoelectronic performance of perovskite materials. So far, replacement of Pb with Sn or Ge has not proved to be a success in terms of air stability, which can be attributed to the apt oxidation of Sn²⁺ and Ge²⁺ in ambient condition [15]. Sb³⁺ instead, with lone pair electrons, exhibits enhanced air stability owing to the screen-charged defects as well as decent photoelectronic property. Despite the fact that lead-free perovskite solar cells suffer from degraded device performance compared with lead containing counterparts, all-inorganic lead-free antimony halide perovskites with a chemical formula of A₃Sb₂X₉

* Corresponding author. Institute of Micro Optoelectronics, Shenzhen University, Room 909, Institute of Micro Optoelectronics, Shenzhen University, Nanshan District, Shenzhen, Guangdong, China.

** Corresponding author.

E-mail addresses: zhaity@hust.edu.cn (T. Zhai), sutinghan@szu.edu.cn (S.-T. Han).

<https://doi.org/10.1016/j.nanoen.2020.104616>

Received 9 December 2019; Received in revised form 6 February 2020; Accepted 11 February 2020

Available online 13 February 2020

2211-2855/© 2020 Elsevier Ltd. All rights reserved.

consisting of corner-shared octahedra inside appears to be applicable substitutes for further study in RS application due to their intrinsic ion migration characteristics and robust ambient stability, which may still outperform other functional materials as RS element.

Beyond that, materials with superb ionic transport property along with the suppression of leakage current are beneficial for the next-generation RS devices. Most active materials applied for RS remain in amorphous (metal oxides) or polycrystalline state. Nevertheless, utilizing amorphous materials with disordered matter and deviation of properties with time is regarded as an intrinsic basis of stochastic variability [16]. Conventional halide perovskites-based RS devices suffer from high leakage and operating current stemmed from the intrinsic nature of polycrystalline film with a great amount of grain boundaries and pin-holes [17]. Single crystal materials which are almost free of pin-holes and grain boundaries affirmatively offer an effective platform for high localization and characterization of the switching events. As yet, single crystalline eco-friendly perovskite material with excellent ionic drift and diffusive properties has not been exerted in the application of RS memory and their electrical characteristics along with the switching mechanism need to be discovered.

During the past few decades, the computing capability of complementary metal oxide semiconductor (CMOS)-based digital computers has been improved greatly due to the continual dimension shrinking of transistors predicted by Moore's law. However, the von Neumann architecture is essentially non-scalable and inefficient in terms of memory, computation and communication [18,19]. Nowadays, there are great efforts on harnessing neuroscientific insights to construct a non von Neumann architecture, composed of artificial neurons and synapses, which is highly efficient with respect to space and energy, and flexible enough to run networks inspired by neural architectures [20–22]. Neural network-based reservoir computing (RC) system was proposed as one alternative of conventional computer architecture to proficiently deal with complex and temporal data such as nonlinear time series in dynamic systems, for instance, speech recognition, classification task and time series prediction [23–26]. In a generalized RC system, the reservoir layer consisting of nonlinear nodes (diffusive RS devices), can process the temporal information which are mapped into a higher dimensional space.

To process temporal information, the reservoir states need to be determined by both present and past inputs within a certain period of time. Therefore, short-term memory is required for the reservoir itself. Short-term synaptic plasticity which refers to information processing in human brain is highly related to the nature of Ca^{2+} dynamics that is, upon the arrival of action potential, the release of neurotransmitters is dominated by Ca^{2+} influx and spontaneous decay at the axon region [27, 28]. In another aspect, authentic diffusive RS devices grounded on ionic migration showing resemblance to the Ca^{2+} dynamics in short-term plasticity and architecture of bio-synapse are barely proposed, which are considered to be superior to the various reported memory devices involving redox reactions of active ions and formation of metal filaments. Thus, successful demonstration of diffusive RS devices with ion dynamics that faithfully emulate of short-term plasticity is urgently required, demonstrating the promising potential for their exploration of further applications in neural network. Hardware system based on ion-modulated diffusive RS devices that natively possess biorealistic properties is expected to offer new capability in artificial neural network which may even facilitate the formulation of neuroscience hypotheses [29–34], in addition to the faithful emulation of short-term dynamics which is urgently required for implementation of RC system as well [35].

In combination of several superiorities, single crystal perovskite material affirmatively offer a platform for systematically apprehending its intrinsic electrical and ionic properties as well as demonstrating high localization and characterization of the switching events with suppressed defects and leakage current [36]. Here, we report monocrySTALLINE lead-free all-inorganic cesium antimony halide perovskite

$\text{Cs}_3\text{Sb}_2\text{Br}_9$ (CSB)-based RS devices and its first experimental implementation in RC system. Both nonvolatile bipolar and volatile threshold switching were achieved by the facile control of the device channel length. A record low electric field of $2.2 \times 10^5 \text{ V m}^{-1}$ for RS event was achieved in the device. The detailed investigation of the physical mechanism of RS revealed that highly mobile Br vacancies ($\text{V}_{\text{Br}}^\bullet$) with low activation energy migrated in defect-free monocrySTALLINE CSB were accounted for the high-performance RS behavior of our device. Besides, short-term plasticity was successfully emulated based on $\text{V}_{\text{Br}}^\bullet$ -mediated diffusion processes which are analogous to the Ca^{2+} influx and spontaneous decay in biological synapses, providing an exhaustive demonstration of intrinsic ionic dynamics as well as corroborating the physical mechanism. The excellent ionic dynamic process of monocrySTALLINE CSB further ensures the diffusive RS devices-based reservoir to process temporal information along with a simple readout function for letter recognition task.

2. Results and discussion

Synthesized CSB with highly crystalline quality is vital to realize high-performance RS devices. The monocrySTALLINE lead-free CSB nanoflakes with submillimeter-size were synthesized by inverse temperature crystallization (ITC) method. The crystal structure of CSB perovskite and the corresponding unit cell where corner-shared $\text{Sb}_2\text{Br}_9^{3-}$ biotetrahedra clusters are surrounded by Cs atoms filling rest of the lattice and neutralizing the negative charges are depicted in Fig. 1a [37]. Confirmed by optical microscope, the as-synthesized CSB monocrySTALLINE nanoflake is uniform with a diameter of 100 μm and corresponding image is shown in Fig. 1b. The atomic force microscope (AFM) image (Fig. S1) depicts the thickness of CSB nanoflake edge is $\sim 100 \text{ nm}$. Fig. 1c shows high-resolution transmission electron microscopy (HRTEM) image. The distinct crystal fringes with lattice spacing of 0.198 nm, corresponding to the (02 $\bar{2}$ 0) and (20 $\bar{2}$ 0) interplanar distance of hexagonal morphology of CSB can be observed [37]. The clear lattice fringe and sharp edges reveal high quality crystalline characteristic of perovskite nanoflakes. Corresponding FFT image of single crystal CSB nanoflakes are shown in Fig. S2.

The X-ray diffraction (XRD) pattern is displayed in Fig. 1d. The main diffraction peaks at 17.8° (002), 27.1° (003), 30.8° (013), 31.5° (222) and 56.4° (006) are confirmed as the characteristic peaks in accordance with the calculated peaks of CSB nanoflakes which is consistent with the space group ($\text{P}\bar{3}\text{m}1$, no. 164) with lattice parameters of $a = 7.9300 \text{ \AA}$, $c = 9.7160 \text{ \AA}$, $\alpha = \beta = 90^\circ$ and $\gamma = 120^\circ$. Moreover, the sharp diffraction peaks imply high crystalline quality of as-synthesized CSB nanoflakes as well. Surface composition information (chemical states) of $\text{Cs}_{3\text{d}}$, $\text{Sb}_{4\text{d}}$ and $\text{Br}_{3\text{d}}$ of CSB were investigated by X-ray photoelectron spectroscopy (XPS) as shown in Fig. S3 and Br-rich distribution at perovskite surface is verified by briefly calculating the elemental ratio (Br/Sb and Br/Cs of approximately 4.77 and 3.70). Coupled peaks at 724.5 eV and 738.5 eV corresponding to $\text{Cs}_{3\text{d}_{5/2}}$ and $\text{Cs}_{3\text{d}_{3/2}}$, doublet peaks at 34.4 eV and 35.6 eV corresponding to $\text{Sb}_{4\text{d}_{5/2}}$ and $\text{Sb}_{4\text{d}_{3/2}}$, and the strong peaks centered at 68.9 eV and 69.7 eV referring to $\text{Br}_{3\text{d}_{5/2}}$ and $\text{Br}_{3\text{d}_{3/2}}$ can be observed. Moreover, the optical properties of monocrySTALLINE CSB nanoflake were characterized by photoluminescence (PL) and UV–visible diffuse reflectance spectra as shown in Fig. 1e. The CSB nanoflakes exhibit an emission peak at 520 nm with a full width at half maximum of 80 nm. An obvious peak emerges from the steady flat line at 500 nm–450 nm and the optical bandgap of 2.39 eV is extracted from the following equation:

$$\alpha h\nu = A(h\nu - E_g)^n \quad (1)$$

where α is the absorption coefficient, h is Planck's constant, ν is the frequency of light, A is constant, E_g is the optical band gap. In this situation, n is 1/2 since CSB nanoflakes are sorted into direct band gap materials. Time resolved PL decay was further carried out to verify exciton recombination dynamics in CSB nanoflake as shown in Fig. 1f

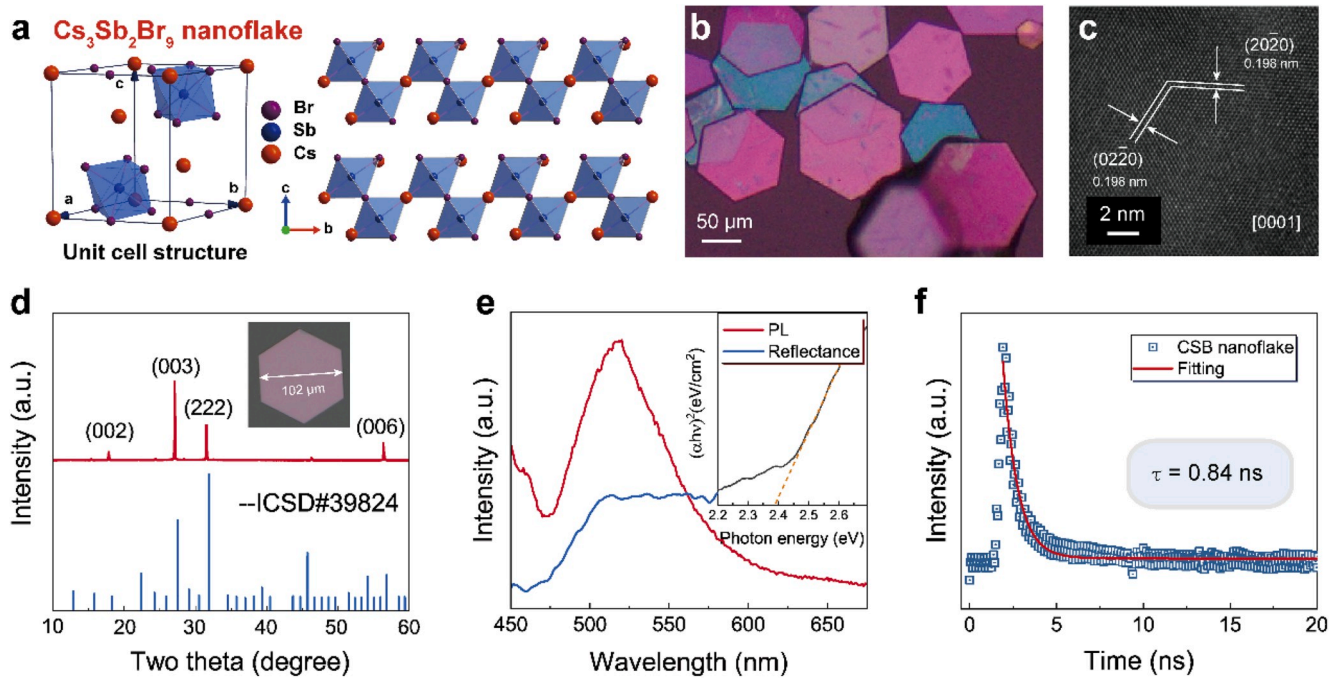


Fig. 1. Characterizations of monocrystalline CSB perovskite nanoflakes.

(a) CSB crystal structure and corresponding unit cell. (b) Photographs of several monocrystalline CSB perovskites taken by optical microscope. (c) HRTEM image of a monocrystalline CSB perovskite. (d) XRD spectra; inset is the photograph of one monocrystalline CSB nanoflake under optical microscope. (e) Reflectance (blue) and PL (red) spectra; inset is the Tauc plot. (f) Time-resolved PL decay and exponential fitting curve.

[38]. By fitting with exponential function, the PL decay displays a mean lifetime τ of 0.84 ns which is originated from exciton radiative recombination [39,40], indicating a high crystalline quality and effectively suppressed nonradiative recombination [41].

We started with a planar structured Au/CSB/Au device in which monocrystalline CSB was contacted with two symmetric inert Au electrodes on $\text{SiO}_2/\text{quartz}$ substrate as depicted in Fig. 2a. CSB based lateral devices were fabricated via direct dripping and crystallization or a dry-transfer strategy. Photographs of CSB device with (upper one) and without (lower one) PVA coverage under optical microscope are shown in Fig. 2b. First, the device behavior was investigated by controlling the channel length. Current-voltage (I - V) measurements of CSB based RS devices with different channel lengths were performed at a fixed compliance current (CC) of 10^{-3} A. The different RS behavior including threshold switching and bipolar RS were observed when channel lengths of CSB RS devices are varied from 1, 2, 5, 10 to 20 μm and the corresponding statistical probability are shown in Fig. 2c. The minimum and maximum channel lengths for reproducible threshold switching and bipolar switching are 10 and 5 μm , respectively. The most reliable threshold switching occurs at a channel length of 10 μm with high probability of 96%.

When the channel length ranges from 1 μm to 5 μm , the CSB RS devices deliver electro-forming free bipolar RS behavior. However, when the channel length is further shortened to 5 μm , the observed higher operation currents may induce deterioration of device electrical performance (Fig. S4b) [42–44]. After applying positive voltage scan on Au electrode, the initial high resistance state (HRS) device was abruptly switched to low resistance state (LRS) with an approximately 10^6 increase in conductance at 2 V (termed the SET process, Fig. S4a) [45]. Afterward, the device was maintained at LRS in the backward scan with increased current to the pre-set CC value. Upon the application of a reversed bias, LRS device was switched back to the initial HRS (termed as RESET process). To further verify the data retention feature of the short channel device (5 μm), retention test was carried out for 2×10^4 s without noticeable fluctuation of on/off ratio (current ratio between LRS and HRS at a reading voltage of 0.5 V), demonstrating outstanding

nonvolatile bipolar RS of the device as shown in Fig. S5.

The device differs substantially in term of resistance transition behavior and threshold switching was observed when the channel length increases to 10 μm although RS devices with longer channel length exhibit unstable switching behaviors (Fig. S4c) [46]. As shown in Fig. 2d, the applied voltage exceeding threshold rapidly switched the device to LRS limited by pre-set CC. Nevertheless, the device spontaneously reinstates to HRS during the backward sweep approaching 0 V. Symmetric hysteresis loop was observed with application of opposite polarity bias, suggesting that the threshold switching is naturally unipolar and significantly different from nonvolatile CSB RS devices with much shorter channel length. Repeatable I - V loops with only positive voltage scan were employed, and the device can spontaneously relax back to HRS without applying an opposite polarity bias. Compared with bulk perovskite active layer in which intrinsic defects exist and ions migration are strongly affected by grain boundaries, the initial HRS current of all measured monocrystalline CSB devices remain at nA level due to the limited number of defect and the absence of grain boundary [14].

Controlling of the CC value is a widely employed approach to realize threshold switching [47]. However, in our case, I - V measurements at different CC ranging from 10^{-3} A to 10^{-7} A (Fig. 2e) confirmed that CSB RS devices exhibit the forming-free threshold switching characteristics regardless of CC value which normally play an important role in tuning the RS behavior [48]. In this case, bipolar RS and threshold switching are realized by tuning the channel length instead of CC values, which might imply a filament-modulated mechanism discussed later. The minimum current point (V_{\min}), the position of voltage where the minimum current is located, serves as one of the most crucial elements commonly observed in threshold switching. Previous studies have denoted that V_{\min} is linearly related to voltage sweeping range due to the oxygen ions migration in Ta_2O_5 -x based memory device [49]. Notably, during the backward voltage scan from 5 V to 0 V in the positive direction, the I - V curves intersect with the x-axis at V_{\min} instead of origin point, implying possible ion migration lowers the net electric field across the active material. The SET voltages of each I - V curve are almost fixed

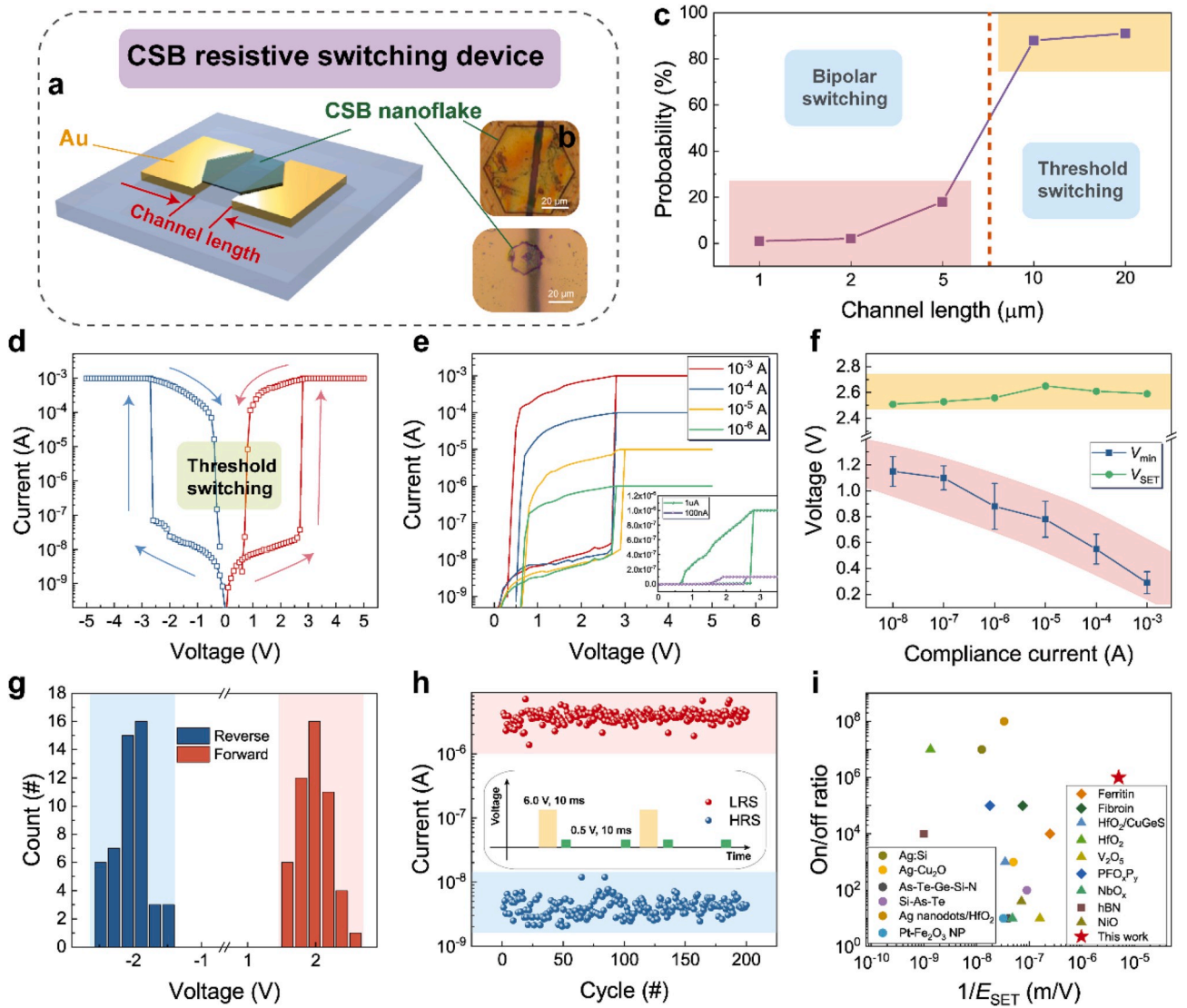


Fig. 2. Electrical characterizations of CSB based memristors.

(a) Schematics of CSB memristor. (b) Photograph of CSB device with (upper one) and without (lower one) PVA coverage under optical microscope. (c) Probability of threshold resistive switching at different channel length. (d) Threshold switching at channel length of 10 μm. (e) Threshold switching at different compliance current. Inset is the switching curve at low compliance current of 1 μA and 100 nA. (f) V_{min} and V_{SET} against compliance current. (g) Statistics of threshold voltages for forward and reverse voltage sweeps. (h) Endurance cycle test of the CSB diffusive memristor. Inset is the applied voltage pulses for the measurement. (i) On/off ratio is plotted against $1/E_{SET}$ for different threshold switching devices.

while evident negative correlation between V_{min} and CC was found, implying the involvement of conductive filament during the threshold switching process (Fig. 2f) [49]. Apparently, a higher CC allows the formation of a more robust conductive filament, likely leading to a much longer data retention time while a thinner conductive filament can be easily ruptured to induce faster relaxation under lower CC. The threshold voltage is positively related to voltage sweep step in which shorter step size contributes to a lower threshold voltage (Fig. S6). The narrow distribution of threshold voltages extracted from consecutive voltage scan at a step of 50 mV (Fig. 2g) verifies the excellent reproducibility of CSB RS devices. Moreover, the CSB RS devices can be cycled for 200 times with distinct separation of HRS/LRS and on/off ratio of over 10^3 (Fig. 2h). No significant variations in current are observed during the switching cycles for both HRS and LRS [50].

Notably, all the electrical measurements were characterized in ambient condition without further encapsulation. The devices were characterized after 30 days which still maintain the RS performance similar to its initial states despite a slight increase in SET voltage

(Fig. S7a). Dry-transfer approach was also utilized for perovskite integration and device fabrication by covering polyvinyl alcohol (PVA) on top of the CSB as an adhesive and protection layer. The introduction of PVA affirmatively enhances the air stability of our device, which further prolongs the storage period up to 60 days without significant performance degradation (Fig. S7b). PVA-based device without CSB nanoflake was also fabricated for comparison and no RS behavior was found as shown in Fig. S7c. The superiority of CSB over conventional organic-inorganic hybrid lead halide perovskites is originated from its intrinsic all-inorganic nature and superb stability of Sb^{3+} [51].

As illustrated in Fig. 2i [47,52–69], by plotting on/off ratio versus electric field of SET operation (E_{SET}), the CSB threshold switching device displays outstanding electrical performance. For threshold switching device with channel length of 10 μm, electrical field of $2.2 \times 10^5 \text{ V m}^{-1}$ is found to be the lowest compared with that of other reported devices as far as we know. For bipolar switching device with channel length of 5 μm, the estimated electric field of $5 \times 10^5 \text{ V m}^{-1}$ is the lowest reported value for lead-free perovskite-based RS devices, which is comparable to

the lowest electric field ($2.5 \times 10^5 \text{ V m}^{-1}$) of lead halide perovskite-based RS memory [70]. It should be mentioned that our device with inert Au electrodes relies on the intrinsic ion migration rather than the electrochemical metallization (ECM) process in the active silver (Ag) electrode-based perovskite RS devices [47,71,72]. Control device with structure of Ag/CSB/Ag exhibits unstable electrical behavior as displayed in Fig. S8.

Assumption that highly mobile ion vacancies with low activation energy migrate in defect-free monocrystalline CSB is accounted for the high performance of our device. Therefore, the volatile RS dynamics stand as a critical role for mechanism study and further applications. The thermodynamically stable V_{Br}^{\bullet} s are easily formed due to its low defect formation energy while Cs and Sb vacancies are hard to be formed under such low electric field since high activation energy are required for the removal of stable Cs from the robust lattice structure and Sb from the octahedral structure. V_{Br}^{\bullet} s only hop within half unit cell, however, migration of Cs and Sb along pathways across one cell severely deteriorate the crystal structure. Corner-sharing $[\text{SbBr}_6]^{3-}$ octahedral structure contributes to easy V_{Br}^{\bullet} s migration between adjacent bromide sites and transport along the equatorial plane under applied electric field by charge carrier hopping process [14,73]. In addition, $\text{Sb}^{0.3d}$ peaks are not observed in XPS spectrum as shown in Fig. S9, indicating that RS behavior only stems from V_{Br}^{\bullet} s migration.

The hypothesized migration path of V_{Br}^{\bullet} s is schematically depicted in Fig. 3a. Under the electrical field, Br^- ions migrate towards anode and conductive filaments consisting V_{Br}^{\bullet} s are formed to bridge the two electrodes which induce the HRS to LRS transition. According to density functional theory (DFT) calculation (Fig. 3b) [14,74], V_{Br}^{\bullet} s can migrate with low activation energy of 0.22 eV which is comparable to that of V_{I}^{\bullet} s in lead halide perovskite and much lower than that of V_{O}^{\bullet} s in oxides [9, 73,75–77], featuring the capability of accomplishing resistance

transition under ultralow electric field. All the measured devices are maintained in insulating state (nA level) due to the limited number of defects in pristine monocrystalline CSB nanoflake while in bulk perovskite films the ions migration are intensely affected by grain boundaries [11,14]. It is noteworthy that the V_{Br}^{\bullet} s filament is highly conductive to allow milliamper operation current at LRS. The more conductive device with larger Joule heating induces right away rupture of conductive filaments [78], recovery to HRS and eventually the volatility of the device. Two competing forces, Soret and Fick forces are taken into account for the filaments shaping and relaxation processes [10]. With the assistance of low external bias and Soret force, V_{Br}^{\bullet} s migrate to form a conductive channel along the temperature gradient. As long as the V_{Br}^{\bullet} s path is completely established, Fick force plays a predominant role to push out the V_{Br}^{\bullet} s from filament region (higher concentration) along the concentration gradient of V_{Br}^{\bullet} s. In general, the relaxation process dominated by Fick force is independent of applied voltage or the direction of electric field. Both bipolar and threshold switching mechanisms are related to the formation and rupture of V_{Br}^{\bullet} s conductive filaments [11,79]. For the devices with channel length shorter than 5 μm , highly localized conductive filaments were formed between the two electrodes during the SET process so that the reverse bias is required to RESET the device to its initial HRS which leads to short-term formation of built-in field within the nanoflake due to the V_{Br}^{\bullet} s accumulation (Fig. 3c and e) [1]. For the devices with longer channel length (more than 10 μm), thinner filaments were formed. The fragile filaments are sensitive to thermally driven force which gives rise to spontaneous transition back to the HRS and threshold switching starting from origin point (Fig. 3d and f).

Energy-dispersive X-ray spectroscopy (EDX) characterizations on CSB nanoflakes were conducted to confirm the migration ion species accounted for RS behavior [11]. Since the formed conductive filaments in threshold switching device spontaneously disrupt in seconds, bipolar

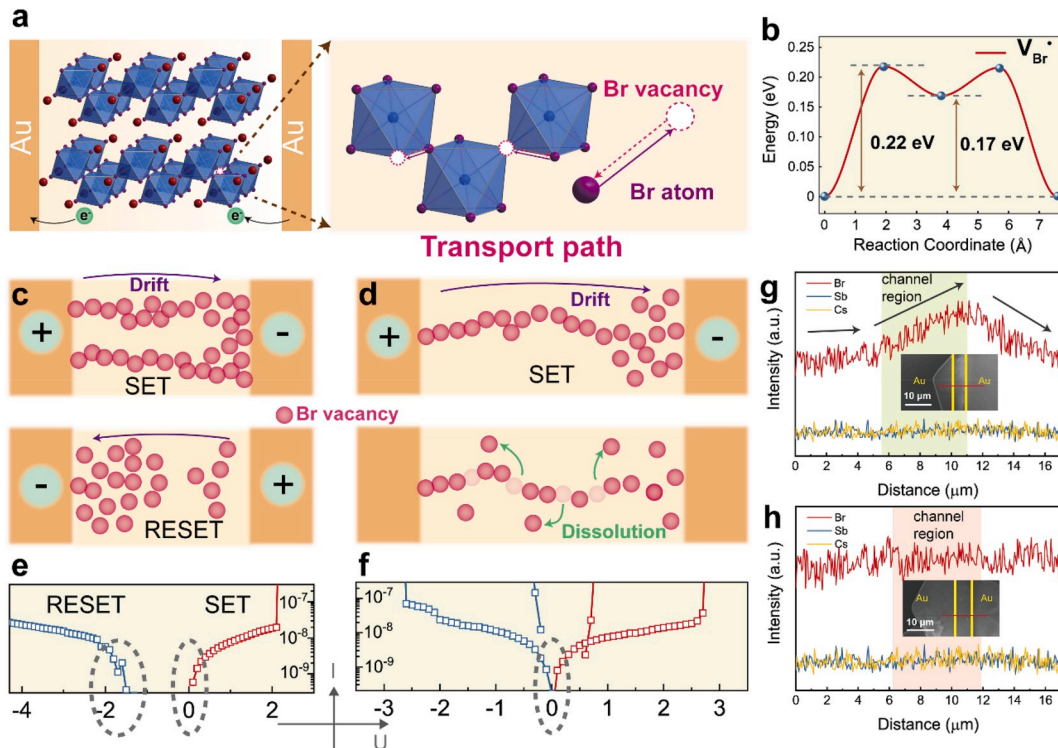


Fig. 3. Operation mechanism for bipolar and threshold resistive switching.

(a) Schematic illustration of bromide vacancy migration path along octahedral edge from one bromide sites to an adjacent one in CSB crystal structure. (b) Activation energy of bromide vacancies through DFT calculation. Bromide vacancy can migrate with low activation energy of 0.22 eV. Migration of Br vacancies for (c) bipolar (shorter channel) and (d) threshold (longer channel) resistive switching devices. Enlarged I - V switching curves at small voltage regime corresponding to (e) bipolar and (f) threshold switching devices. EDX line scan profiles of CSB nanoflakes (g) with and (h) without the application of voltage. Positive voltage was applied to the right Au electrode.

resistive devices with short channel length were employed for this characterization. Upon the application of positive voltage to the right Au electrode, the CSB RS device with channel length of 5 μm was pre-programmed to LRS which can maintain for a long time due to the intrinsic nonvolatile property. Br^- ions were driven towards the positively biased right Au electrode, resulting in the growth of V_{Br} s conductive paths. This process was verified by EDX line scan across CSB nanoflake parallel to the direction of electrodes, as illustrated in Fig. 3g. The recorded spectra were normalized against the maximum intensity of Br. The Br intensity appears to increase along the direction opposite to the pre-applied electric field, while the intensities of Sb and Cs retain almost unchanged across the CSB nanoflake. Similar characteristic was found in other five devices with the same channel length and amplitude of applied voltage. For CSB nanoflakes without SET operation, homogeneous distribution of Br was observed (Fig. 3h) which unambiguously verified that Br ions (vacancies) act as the only migrated species under external electric field.

Short-term dynamics is important for the implementation of hardware-based reservoir computing in RC networks, which sparks requirement on diffusive device with ionic dynamics. In the following, we take full advantage of high mobility of V_{Br} s in CSB RS devices to emulate short-term plasticity related to Ca^{2+} dynamics in biological synapses as schematically depicted in Fig. 4a [21,28,80,81]. Upon the arrival of action potentials at the axon terminal, voltage gated Ca^{2+} channels are excited, resulting in the Ca^{2+} influx inside presynaptic membrane from synaptic cleft [82]. In consequence, the release of neurotransmitters from synaptic vesicles and the following advent at postsynaptic terminal leads to the enhancement of the connection strength (synaptic weight) between pre- and post-synaptic neurons [83]. The recovery of Ca^{2+} concentration takes place via the extrusion through plasma membrane back to the synaptic cleft. Similarly, upon the arrival of input voltage stimuli, V_{Br} s within CSB threshold switching

device with diffusive-relaxation dynamics lead to transient enhancement in conductivity [84], followed by a spontaneous decay to the initial state [85]. Although numerous researches have focused on the pulse-induced excitement process, relaxation process which is vital to RC application was not paid sufficient attention. During pulse measurements, the current state of the CSB RS devices can be well tuned by varying the pulse parameters including amplitude and frequency [86, 87].

To demonstrate temporal dynamics of the CSB threshold switching device (10 μm length channel), electrical pulses with amplitude ranging from 5 V, 6 V–7 V for 1 ms are applied to the device and the response of the device is characterized by the read current. Postsynaptic current (PSC), represented by the lateral current between two electrodes can be well modulated via the regulation of the V_{Br} s filament. As illustrated in Fig. 4b, by applying electrical pulse, a substantial change in synaptic weight by orders of magnitude can be observed in our device. The following spontaneous relaxation process induced by the redistribution of V_{Br} and rupture of formed filament allow the device to transit back to its insulating state (relaxation time τ of 0.6 s for 6 V pulse). The relaxation time increases with increasing pulse amplitude. It should be noted that the pulse width (1 ms) is comparably short for lateral device with a channel length of 10 μm and a characteristic relaxation time of hundreds μs is observed. Therefore, the mobile ionic species responsible for short-term plasticity is V_{Br} rather than V_{Cs} since activation energy of V_{Cs} is much higher than the value of V_{Br} which is not capable of accomplishing instantaneous responses on such short timescales (ms level). Fig. 4c demonstrates the frequency-dependent response to write pulse with fixed amplitude (6 V, 1 ms) and different timeframes [88]. The current soon decays back to the original resting state when the pulse frequency is low since there is not enough stimulation during this period, while the response will gradually increase when multiple pulses are applied within short intervals (high frequency), showing an accumulation effect of V_{Br} s

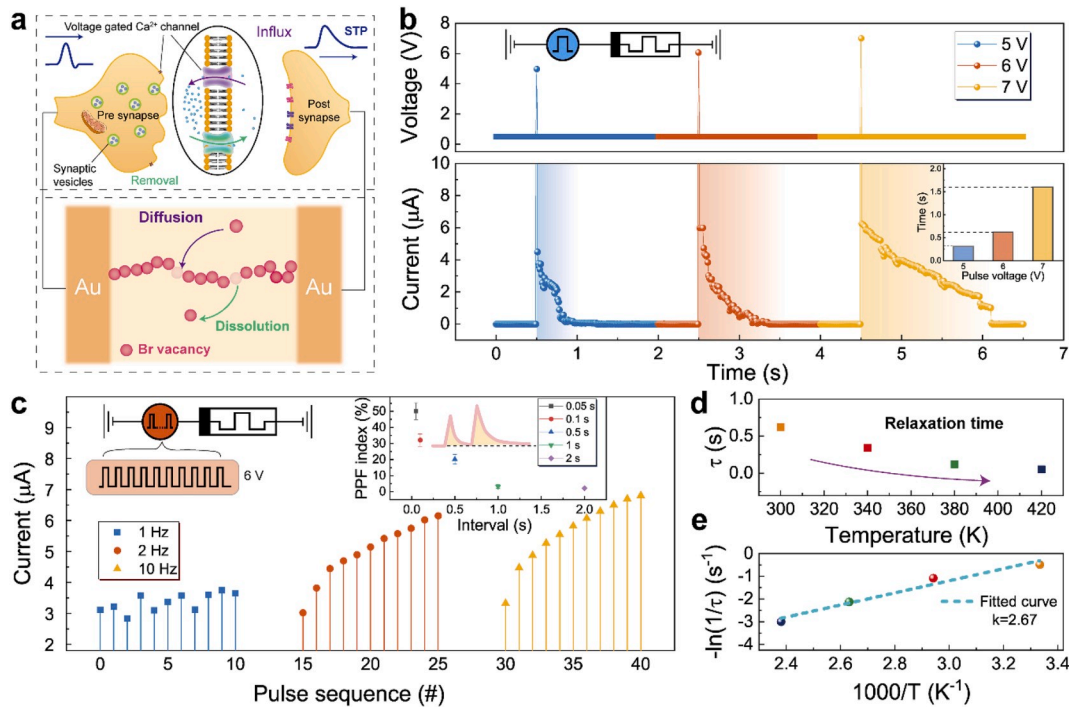


Fig. 4. Analogy between bio-synapses and CSB diffusive memristors and short-term dynamics under pulse stimuli.

(a) Schematics of Ca^{2+} and Br vacancy dynamics in synapses and between electrodes, respectively. The upper part represents the influx and removal of Ca^{2+} through channels on plasma membrane. The bottom part shows the diffusion of Br vacancy and spontaneous dissolution of the conductive filaments after the removal of voltage stimuli. (b) Measured current responses under input voltage pulse with different amplitudes (5 V, 6 V, 7 V) and the following relaxation process. Inset shows the relaxation time under different amplitudes. (c) Current response of CSB diffusive memristor to pulse sequence with different input pulse frequencies showing PPF behavior (short-term plasticity). Inset is the PPF index in percentage at different pulse intervals. (d) Relaxation time at different temperature. (e) Device current decay time was plotted in form of $-\ln(1/\tau)$ against $1/kT$. The diffusion activation energy extracted from Arrhenius plot is calculated to be 0.23 eV.

ion, in analogy with the paired pulse facilitation (PPF) in biological synapses. PPF index as a function of interval time of paired pulses is plotted in the inset of Fig. 4c [89].

In order to understand the ion migration dynamics, the CSB RS devices were switched under 300 K–420 K. As shown in Fig. 4d, the relaxation time is inversely related to temperature since the Joule heating can break the filament at high temperature at shorter timescale (current decay at different temperatures was shown in Fig. S11). Analogous to V_{Br}^* s, spontaneous diffusion of V_{Br}^* s from the filament region results in the decrease in V_{Br}^* concentration which can be expressed related to time t [90,91]:

$$N = \frac{N_{Br}}{\sqrt{\pi Dt}} \exp\left(-\frac{x^2}{4Dt}\right) \quad (2)$$

where N_{Br} is the total number of V_{Br}^* within one CSB nanoflake, x is the position away from the center of the filament and D represents the diffusion coefficient. D can be expressed as

$$D = D_0 \exp\left(-\frac{E_a}{k_B T}\right) \quad (3)$$

where D_0 is the maximum diffusion coefficient at infinite temperature, E_a is the diffusion activation energy for V_{Br}^* migration and k_B is Boltzmann constant. As for the monocrystalline CSB nanoflake, the initial V_{Br}^* concentration is neglected. During the relaxation process within decay time τ , the V_{Br}^* concentration should drop below the critical $N^* = \frac{N_{Br}}{\sqrt{\pi D \tau}}$.

$$\tau = \frac{1}{\pi D_0} \left(\frac{N_{Br}}{N^*}\right)^2 \exp\left(\frac{E_a}{k_B T}\right) \quad (4)$$

This expression can be simplified as:

$$C + \ln\left(\frac{1}{\tau}\right) = -\frac{E_a}{k_B T} \quad (5)$$

where C is a fitting parameter, τ is the current decay time at given temperature T . Diffusion energy can then be obtained by plotting this equation. Current decay time was plotted in form of $-\ln(1/\tau)$ against $1/kT$ to analyze the migration dynamics as shown in the inset in Fig. 4e [92,93]. The linear region is observed from the Arrhenius plot within all temperature range. Besides, low activation energy E_a was extracted to be 0.23 eV by linearly fitting the plot (Eq. (5)), indicating V_{Br}^* s is likely to be the only responsive species for ion migration. Here, it should be pointed out that current decay can hardly be recorded due to the greatly suppressed ion migration and charge carrier transport processes at low temperature condition [94]. The ion migration rate can be estimated by the following equation:

$$k = \frac{k_B T}{h} e^{-\frac{E_a}{k_B T}} \quad (6)$$

where h and R represent the reduced Planck constant and ideal gas constant, respectively. The migration rate is roughly calculated to be $1.2 \times 10^9 \text{ s}^{-1}$ at room temperature under the guidance of energy profiles for V_{Br}^* s migration. V_{Br}^* s migrate towards random direction within CSB nanoflake without external electric field while V_{Br}^* s tend to migrate along the electrical field direction under external bias. According to Fig. S10, activation energy of V_{Br}^* s decreases along the target electrodes direction owing to the stabilization force once V_{Br}^* s reach the electrode while an energy penalty should be taken into account in the reverse direction. Hundreds of microseconds are required for V_{Br}^* s to reach target electrode (detailed in Supporting Information), close to the time required for driving a RS event which is also a proof that V_{Br}^* s are the only possible mobile species [95].

On the basis of the previously mentioned characteristics of short-term memory with analogous Ca^{2+} dynamics, CSB diffusive RS devices possess the ability of mapping input signals to high dimensional states by performing nonlinear transformation. Besides, the diffusive RS

devices well possess the ability to distinguish input sequences with different temporal order, which can be appropriately applied for pattern classification task. Therefore, with the desired and intriguing properties, the implementation of RC system in which the reservoir layer was composed of monocrystalline perovskite-based RS devices with tunable ionic dynamics was firstly proposed for classification task. The RC system consists of three sections including the input layer, reservoir layer and the output layer, as schematically illustrated in Fig. 5a. The reservoir processing layer is connected to the input layer with a fixed weight (unit value), showing no demand for weight update (training). As first part of RC system, the ‘reservoir’ composed of dynamic CSB diffusive RS devices can perform nonlinear transformation to process the temporal information $u(t)$ from input layer into a higher dimensional space $x(t)$ [26]. The connectivity construction of reservoir is fixed while the neurons in reservoir develop dynamically with the temporal input signal. Transient current responses are generated under input signals to serve as reservoir states which are then analyzed by the second part of RC system, ‘readout function’. Final output $y(t)$ can be generated through simple readout function of a linear combination of the reservoir states, depending on the connection weights which evolves upon each train (carried out in software Matlab). Compared with recurrent neural network (RNN), RC system with a dynamic diffusive RS devices-based reservoir and a simple readout function has fewer connection weights to be updated so that the training cost can be reduced significantly [23, 26].

As discussed above, the interval time between the application of adjacent pulses affects current state (reservoir state $x(t)$) of the CSB diffusive RS devices, enabling pulse sequences with various temporal order to be distinctly separated from each other, which further allows the realization of letter recognition task by exploiting the short-term potentiation feature of the CSB diffusive RS devices. To perform letter recognition, we first dealt with the input patterns (four letters “FMGE”, short for our research group “Functional Materials & Electronics Group”), which were treated as pixels with size of 5 rows \times 5 columns, containing only purple (considered as 1) and white (considered as 0) ones as depicted in Fig. 5b. In the following process, each pixel-based pattern was split into 5 temporal pulse sequences by row to be delivered into the five selected RS devices that constitute the reservoir layer. Within one temporal pulse sequence, program pulse (6 V, 1 ms) and read voltage (0.5 V) are arranged with an interval time of 0.5 s according to the binary sequence. Taking letter “M” as an example, the first temporal sequence is presented as “10001”, dictated by the spatial distribution of purple pixels (two purple squares at both ends illustrated by the dashed square), and was fed into the first device #1 (Fig. 5c). Letter “F”, “E” and “G” were also listed along with their input pulse sequences divided into each row and corresponding current responses after pulse sequence application for individual diffusive RS devices are shown in Fig. S12. It is worth noting that two pulses were included in this pulse sequence (“10001”), however, the exact time nodes that the pulse voltage is applied is of critical importance since the input pattern has to be appropriately prepared and processed nothing but the precise order of pulse application. Upon the arrival of pulse sequences, the resistance of the CSB diffusive RS devices changes relying on the temporal order that is originated from the input pattern.

Benefiting from the hardware processing of CSB device to handle the temporal pulse sequence (row), the resulting reservoir state $x(t)$ contains information of spatially distributed pattern. The RC architecture in this work requires a network of a limited size (5×4) without a hidden layer for letter recognition, leaving only 20 connection weights to be updated during each training operation (Fig. 5c). For the chosen four letters “F”, “M”, “E” and “G”, each composed of 25 (5×5) pixels, six basic pulse sequences of different order are extracted for the combination of the four given letters. The current response of CSB diffusive RS devices to the obtained six pulse sequences was shown in Fig. 5e, which demonstrate the distinct response to each pulse sequence with sufficient margin to be separated. Furthermore, four different pulse sequences each with two

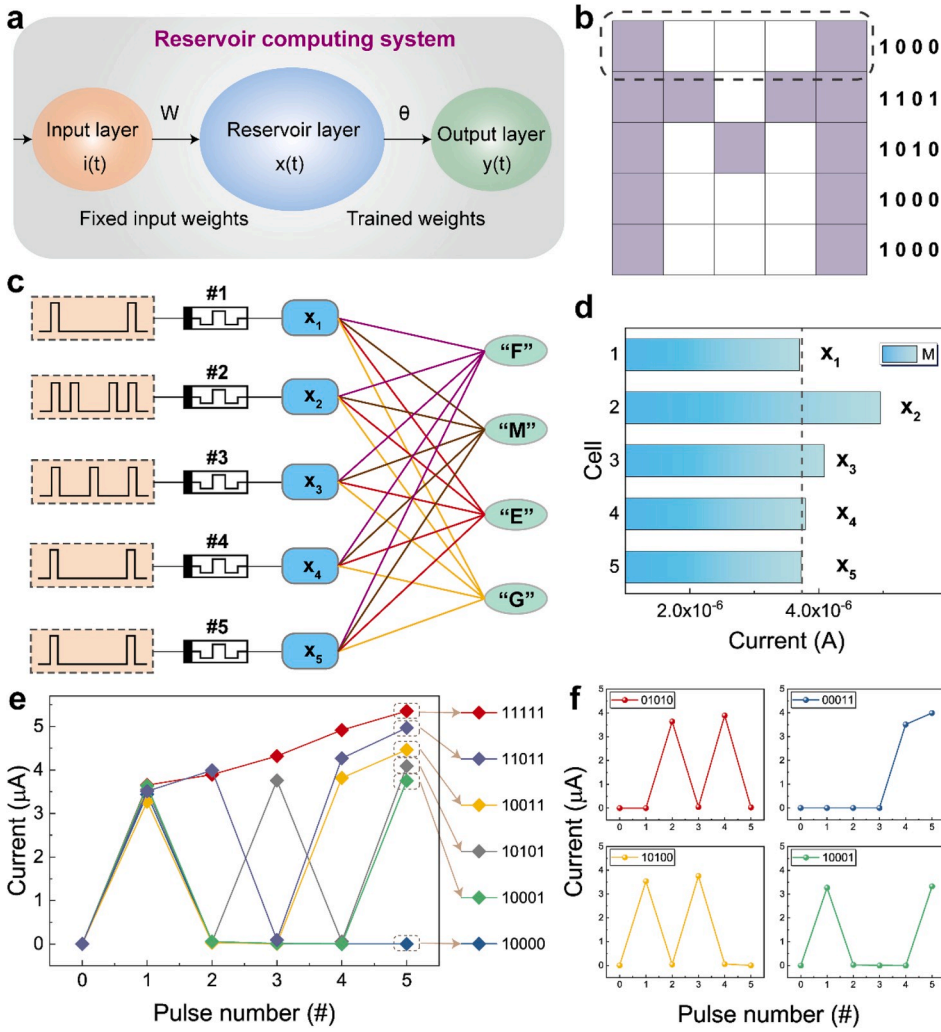


Fig. 5. RC system based on CSB memristors.

(a) Three layers including the input layer, reservoir layer and output layer and corresponding input $i(t)$, reservoir state $x(t)$ and output $y(t)$, respectively. Input weights stay fixed while weights connecting reservoir and output layer require training process. (b) Letter "M" as an example with size of 5 pixels \times 5 pixels for letter recognition. The first temporal sequence is presented as '10001' as depicted in the dashed rectangle. (c) RC system based on five CSB diffusive memristors. Input pulse sequences were fed into the memristors and corresponding reservoir states x_i were recorded, respectively. (d) Each recorded reservoir states for input letter "M". (e) Current response to each individual pulse of six basic pulse sequences. (f) Current response to each individual pulse of four selected pulse sequences each of which contains two "1" with different order.

"1" were fed in to the CSB RS devices and resulted in different current response, indicating the capability of identifying temporal order of input data (Fig. 5f). After the RC system was successfully trained and all training samples were perfectly recognized and classified with recognition accuracy of over 96%. Notably, testing samples differ from the training samples manifesting as the addition of noise pixels by replacing the original one with the opposite and have not been used for training event before to verify the feasibility of the network (Fig. S13). Owing to the distinguishable feature on temporal input signals of the RC system, letter recognition was successfully performed for test samples, where test sample pattern #1, #2, #3 and #4 are properly classified into letter "F" "M" "E" and "G" in the readout function, respectively, revealing the outstanding performance of the trained RC system based on CSB diffusive RS devices with the ability of temporal information processing. Training samples illustrated in right part of Fig. S13 can hardly be recognized since they can be regarded as either "E" or "F", or even something in between. More complicated tasks such as bio-signal processing and disease detection may be implemented by employing multitude diffusive RS devices and certainly require an advanced network scheme for computing efficiency.

3. Conclusion

In summary, we proposed for the first time a monocrySTALLINE lead-free $\text{Cs}_3\text{Sb}_2\text{Br}_9$ nanoflake based lateral-structured device with nonvolatile bipolar and volatile threshold switching characteristics by varying

the channel length as a memristive platform to study the underlying mechanism and dynamic process. A record-low electric field of $2.2 \times 10^5 \text{ V m}^{-1}$ for threshold switching is achieved, stemming from V_{BTS} migration with low activation energy in defects-free monocrySTALLINE CSB which is confirmed by DFT, EDX and temperature-dependent experiment. V_{BTS} mediated CSB diffusive RS devices were further employed for the emulation of short-term plasticity, similar to the Ca^{2+} influx and spontaneous decay processes in the biological counterparts, and implemented as the reservoir element for spatial temporal data processing, along with a simple readout function to form an energy efficient reservoir computing system for letter recognition task, which offers promising strategy for building hardware efficient and simplified neuromorphic computing architecture.

4. Experimental section

Synthesis of CSB Perovskite Nanoflakes. CSB perovskite nanoflakes were prepared using inverse temperature crystallization (ITC) method. Cesium bromide (CsBr) and bromide antimony (SbBr_3) were dissolved into hydrobromic acid (HBr) solvent with a mole ratio of 3:2 at 130°C to prepare the precursor solution. CSB nanoflakes were synthesized through the attachment of dissociative Br from CsBr to the extended SbBr_3 octahedral network as terminal groups to form a hexagonal cell. After dripped on quartzes substrates, CSB perovskite nanoflakes successfully crystallized at 140°C for the evaporation of HBr .

Device fabrication. Photolithography was employed to pattern the

planar electrode structure with long channel length and short channel ($<5\ \mu\text{m}$) was patterned via e-beam lithography techniques. Ti/Au symmetric electrodes with a thickness of 3/90 nm were then deposited on quartz or SiO_2 substrate. The single crystal CSB RS devices were then fabricated via direct dripping and crystallization or a dry-transfer strategy on deposited bottom planar electrodes. Dry-transfer strategy was carried out for device protection against atmospheric condition through sticking the prepared CSB nanoflake with a small piece of PVA film (about $2\ \text{mm} \times 2\ \text{mm}$), followed by the alignment and transfer onto pre-patterned channel region under optical microscope.

Characterization of CSB nanoflakes and RS devices. The surface morphology was recorded by optical microscope (BX51, OLMPUS) and the thickness of the synthesized nanoflakes was measured by an atomic force microscope (Dimension Icon, Bruker). The crystal structure of CSB perovskite nanoflakes was characterized by transmission electron microscope (Tecnai F30) and X-ray diffraction (XRD) (Empyrean, PANalytical B.V.). The diffuse reflectance was recorded by an UV-vis spectrophotometer (U-3900H, Hitachi). The chemical state was analyzed by X-ray photoelectron spectroscopy (AXIS-ULTRA DLD-600W, Kratos). Confocal Raman spectroscopy (ALPHA300 RAS, WITec) with a pulsing 355 nm laser was employed for the measurement of photoluminescence (PL) decay curve. Field-emission scanning electron microscope (SEM) images of the CSB RS device was captured by a field emission scanning electron microscope (Carl Zeiss MERLIN Compact), and Energy dispersive X-ray spectroscopy (EDX) line scan was conducted by the Bruker XFlash 6[10]. Electrical measurements were conducted on the symmetric device and I - V characteristics were measured using a Keithley 4200-SCS semiconductor parameter analyzer, Keysight B1500A parameter analyzer and Keysight B2902A precision source/measure unit at ambient condition.

Declaration of competing interest

The authors declare that they have no known competing financial interests or personal relationships that could have appeared to influence the work reported in this paper.

Acknowledgements

J.-Y. M and Z. Z contributed equally to this work. The authors acknowledge the grants from the National Natural Science Foundation of China (21801081, 21825103, 61974093 and 51902205), the China Postdoctoral Science Foundation (2017M622434, 2019T120646), Guangdong Province Special Support Plan for High-Level Talents (Grant No. 2017TQ04X082), Guangdong Provincial Department of Science and Technology (Grant No. 2018B030306028), the Science and Technology Innovation Commission of Shenzhen (Grant Nos. JCYJ20180507182042530, JCYJ20180507182000722 and JCYJ20180305125314948), Shenzhen Peacock Technological Innovation Project (Grant Nos. KQJSCX20170727100433270).

Appendix A. Supplementary data

Supplementary data to this article can be found online at <https://doi.org/10.1016/j.nanoen.2020.104616>.

References

- [1] Z. Xiao, Y. Yuan, Y. Shao, Q. Wang, Q. Dong, C. Bi, P. Sharma, A. Gruverman, J. Huang, Giant switchable photovoltaic effect in organometal trihalide perovskite devices, *Nat. Mater.* 14 (2015) 193–198.
- [2] C. Eames, J.M. Frost, P.R. Barnes, B.C. O'Regan, A. Walsh, M.S. Islam, Ionic transport in hybrid lead iodide perovskite solar cells, *Nat. Commun.* 6 (2015) 7497.
- [3] J.M. Azpiroz, E. Mosconi, J. Bisquert, F. De Angelis, Defect migration in methylammonium lead iodide and its role in perovskite solar cell operation, *Energy Environ. Sci.* 8 (2015) 2118–2127.
- [4] W. Tress, Metal halide perovskites as mixed electronic-ionic conductors: challenges and opportunities-from hysteresis to memristivity, *J. Phys. Chem. Lett.* 8 (2017) 3106–3114.
- [5] H.L. Ma, W. Wang, H.Y. Xu, Z.Q. Wang, Y. Tao, P. Chen, W.Z. Liu, X.T. Zhang, J. G. Ma, Y.C. Liu, Interface state-induced negative differential resistance observed in hybrid perovskite resistive switching memory, *ACS Appl. Mater. Interfaces* 10 (2018) 21755–21763.
- [6] O.S. Game, G.J. Buchsbaum, Y. Zhou, N.P. Padture, A.I. Kingon, Ions matter: description of the anomalous electronic behavior in methylammonium lead halide perovskite devices, *Adv. Funct. Mater.* 27 (2017) 1606584.
- [7] J.S. Han, Q.V. Le, J. Choi, K. Hong, C.W. Moon, T.L. Kim, H. Kim, S.Y. Kim, H. W. Jang, Air-stable cesium lead iodide perovskite for ultra-low operating voltage resistive switching, *Adv. Funct. Mater.* 28 (2018) 1705783.
- [8] F. Zhou, Y. Liu, X. Shen, M. Wang, F. Yuan, Y. Chai, Low-voltage, optoelectronic $\text{CH}_3\text{NH}_3\text{PbI}_3\text{-xCl}_x$ memory with integrated sensing and logic operations, *Adv. Funct. Mater.* 28 (2018) 1800080.
- [9] J. Choi, S. Park, J. Lee, K. Hong, D.H. Kim, C.W. Moon, G.D. Park, J. Suh, J. Hwang, S.Y. Kim, H.S. Jung, N.G. Park, S. Han, K.T. Nam, H.W. Jang, Organolead halide perovskites for low operating voltage multilevel resistive switching, *Adv. Mater.* 28 (2016) 6562–6567.
- [10] K. Kang, H. Ahn, Y. Song, W. Lee, J. Kim, Y. Kim, D. Yoo, T. Lee, High-performance solution-processed organo-metal halide perovskite unipolar resistive memory devices in a cross-bar array structure, *Adv. Mater.* 31 (2019) 1804841.
- [11] X. Zhu, J. Lee, W.D. Lu, Iodine vacancy redistribution in organic-inorganic halide perovskite films and resistive switching effects, *Adv. Mater.* 29 (2017) 1700527.
- [12] G. Lin, Y. Lin, R. Cui, H. Huang, X. Guo, C. Li, J. Dong, X. Guo, B. Sun, An organic-inorganic hybrid perovskite logic gate for better computing, *J. Mater. Chem. C* 3 (2015) 10793–10798.
- [13] J.S. Han, Q.V. Le, J. Choi, H. Kim, S.G. Kim, K. Hong, C.W. Moon, T.L. Kim, S. Y. Kim, H.W. Jang, Lead-free all-inorganic cesium tin iodide perovskite for filamentary and interface-type resistive switching toward environment-friendly and temperature-tolerant nonvolatile memories, *ACS Appl. Mater. Interfaces* 11 (2019) 8155–8163.
- [14] C. Cuhadar, S.G. Kim, J.M. Yang, J.Y. Seo, D. Lee, N.G. Park, All-inorganic bismuth halide perovskite-like materials $\text{A}_3\text{Bi}_2\text{I}_9$ and $\text{A}_3\text{BiI}_8\text{Na}_0.2\text{I}_8.6$ ($\text{A} = \text{Rb}$ and Cs) for low-voltage switching resistive memory, *ACS Appl. Mater. Interfaces* 10 (2018) 29741–29749.
- [15] M.H. Kumar, S. Dharani, W.L. Leong, P.P. Boix, R.R. Prabhakar, T. Baikie, C. Shi, H. Ding, R. Ramesh, M. Asta, M. Graetzel, S.G. Mhaisalkar, N. Mathews, Lead-free halide perovskite solar cells with high photocurrents realized through vacancy modulation, *Adv. Mater.* 26 (2014) 7122–7127.
- [16] E.J. Yoo, M. Lyu, J.H. Yun, C.J. Kang, Y.J. Choi, L. Wang, Resistive switching behavior in organic-inorganic hybrid $\text{CH}_3\text{NH}_3\text{PbI}_3\text{-xCl}_x$ perovskite for resistive random access memory devices, *Adv. Mater.* 27 (2015) 6170–6175.
- [17] Y. Shao, Y. Fang, T. Li, Q. Wang, Q. Dong, Y. Deng, Y. Yuan, H. Wei, M. Wang, A. Gruverman, J. Shield, J. Huang, Grain boundary dominated ion migration in polycrystalline organic-inorganic halide perovskite films, *Energy Environ. Sci.* 9 (2016) 1752–1759.
- [18] J.J. Yang, D.B. Strukov, D.R. Stewart, Memristive devices for computing, *Nat. Nanotechnol.* 8 (2013) 13–24.
- [19] D. Ielmini, H.S.P. Wong, In-memory computing with resistive switching devices, *Nat. Electron* 1 (2018) 333–343.
- [20] L.Q. Zhu, C.J. Wan, L.Q. Guo, Y. Shi, Q. Wan, Artificial synapse network on inorganic proton conductor for neuromorphic systems, *Nat. Commun.* 5 (2014) 3158.
- [21] B. Gao, Y. Bi, H.-Y. Chen, R. Liu, P. Huang, B. Chen, L. Liu, X. Liu, S. Yu, H.S. P. Wong, J. Kang, Ultra-low-energy three-dimensional oxide-based electronic synapses for implementation of robust high-accuracy neuromorphic computation systems, *ACS Nano* 8 (2014) 6998–7004.
- [22] D.S. Jeong, C.S. Hwang, Nonvolatile memory materials for neuromorphic intelligent machines, *Adv. Mater.* 30 (2018) 1704729.
- [23] C. Du, F. Cai, M.A. Zidan, W. Ma, S.H. Lee, W.D. Lu, Reservoir computing using dynamic memristors for temporal information processing, *Nat. Commun.* 8 (2017) 2204.
- [24] Y. Li, L. Xu, Y.-P. Zhong, Y.-X. Zhou, S.-J. Zhong, Y.-Z. Hu, L.O. Chua, X.-S. Miao, Associative learning with temporal contiguity in a memristive circuit for large-scale neuromorphic networks, *Adv. Electron. Mater.* 1 (2015) 1500125.
- [25] W. Wang, G. Pedretti, V. Milo, R. Carboni, A. Calderoni, N. Ramaswamy, A. S. Spinelli, D. Ielmini, Learning of spatiotemporal patterns in a spiking neural network with resistive switching synapses, *Sci. Adv.* 4 (2018) eaat4752.
- [26] L. Appeltant, M.C. Soriano, G. Van der Sande, J. Danckaert, S. Massar, J. Dambre, B. Schrauwen, C.R. Mirasso, I. Fischer, Information processing using a single dynamical node as complex system, *Nat. Commun.* 2 (2011) 468.
- [27] D.E. Clapham, Calcium Signaling, *Cell* 131 (2007) 1047–1058.
- [28] R.S. Zucker, W.G. Regehr, Short-term synaptic plasticity, *Annu. Rev. Physiol.* 64 (2002) 355–405.
- [29] D. Kuzum, S. Yu, H.S. Wong, Synaptic electronics: materials, devices and applications, *Nanotechnology* 24 (2013) 382001.
- [30] L.F. Abbott, S.B. Nelson, Synaptic plasticity: taming the beast, *Nat. Neurosci.* 3 (2000) 1178.
- [31] L. Zhou, J.Y. Mao, Y. Ren, J.Q. Yang, S.R. Zhang, Y. Zhou, Q. Liao, Y.J. Zeng, H. Shan, Z. Xu, J. Fu, Y. Wang, X. Chen, Z. Lv, S.T. Han, V.A.L. Roy, Biological spiking synapse constructed from solution processed bimetal core-shell nanoparticle based composites, *Small* 14 (2018) 1800288.
- [32] X. Yan, Y. Pei, H. Chen, J. Zhao, Z. Zhou, H. Wang, L. Zhang, J. Wang, X. Li, C. Qin, G. Wang, Z. Xiao, Q. Zhao, K. Wang, H. Li, D. Ren, Q. Liu, H. Zhou, J. Chen,

- P. Zhou, Self-assembled networked PbS distribution quantum dots for resistive switching and artificial synapse performance boost of memristors, *Adv. Mater.* 31 (2018) 1805284.
- [33] C. Wu, T.W. Kim, H.Y. Choi, D.B. Strukov, J.J. Yang, Flexible three-dimensional artificial synapse networks with correlated learning and trainable memory capability, *Nat. Commun.* 8 (2017) 752.
- [34] L. Wang, Z. Wang, W. Zhao, B. Hu, L. Xie, M. Yi, H. Ling, C. Zhang, Y. Chen, J. Lin, J. Zhu, W. Huang, Controllable multiple depression in a graphene oxide artificial synapse, *Adv. Electron. Mater.* 3 (2017) 1600244.
- [35] R. Waser, M. Aono, Nanoionics-based resistive switching memories, *Nat. Mater.* 6 (2007) 833–840.
- [36] G. Milano, M. Luebben, Z. Ma, R. Dunin-Borkowski, L. Boarino, C.F. Pirri, R. Waser, C. Ricciardi, I. Valov, Self-limited single nanowire systems combining all-in-one memristive and neuromorphic functionalities, *Nat. Commun.* 9 (2018) 5151.
- [37] J. Zhang, Y. Yang, H. Deng, U. Farooq, X. Yang, J. Khan, J. Tang, H. Song, High quantum yield blue emission from lead-free inorganic antimony halide perovskite colloidal quantum dots, *ACS Nano* 11 (2017) 9294–9302.
- [38] J. Song, J. Li, L. Xu, J. Li, F. Zhang, B. Han, Q. Shan, H. Zeng, Room-temperature triple-ligand surface engineering synergistically boosts ink stability, recombination dynamics, and charge injection toward EQE-11.6% perovskite QLEDs, *Adv. Mater.* 30 (2018) 1800764.
- [39] D. Yang, X. Li, W. Zhou, S. Zhang, C. Meng, Y. Wu, Y. Wang, H. Zeng, CsPbBr₃ quantum dots 2.0: benzenesulfonic acid equivalent ligand awakens complete purification, *Adv. Mater.* 31 (2019) 1900767.
- [40] M.V. Kovalenko, L. Manna, A. Cabot, Z. Hens, D.V. Talapin, C.R. Kagan, V. I. Klimov, A.L. Rogach, P. Reiss, D.J. Milliron, P. Guyot-Sionnest, G. Konstantatos, W.J. Parak, T. Hyeon, B.A. Korgel, C.B. Murray, W. Heiss, Prospects of nanoscience with nanocrystals, *ACS Nano* 9 (2015) 1012–1057.
- [41] Z. Zheng, X. Wang, Y. Shen, Z. Luo, L. Li, L. Gan, Y. Ma, H. Li, A. Pan, T. Zhai, Space-confined synthesis of 2D all-inorganic CsPbI₃ perovskite nanosheets for multiphoton-pumped lasing, *Adv. Opt. Mater.* 6 (2018) 1800879.
- [42] J.-M. Yang, E.-S. Choi, S.-Y. Kim, J.-H. Kim, J.-H. Park, N.-G. Park, Perovskite-related (CH₃NH₃)₃Sb₂Br₉ for forming-free memristor and low-energy-consuming neuromorphic computing, *Nanoscale* 11 (2019) 6453–6461.
- [43] J. Ge, S. Zhang, Z. Liu, Z. Xie, S. Pan, Flexible artificial nociceptor using a biopolymer-based forming-free memristor, *Nanoscale* 11 (2019) 6591–6601.
- [44] J. Zheng, J. Zhang, Z. Wang, L. Zhong, Y. Sun, Z. Liang, Y. Li, L. Jiang, X. Chen, L. Chi, Programmable negative differential resistance effects based on self-assembled Au@PPy core-shell nanoparticle arrays, *Adv. Mater.* 30 (2018) 1802731.
- [45] A. Rani, D.B. Velusamy, F. Marques Mota, Y.H. Jang, R.H. Kim, C. Park, D.H. Kim, One-step all-solution-based Au-GO core-shell nanosphere active layers in nonvolatile ReRAM devices, *Adv. Funct. Mater.* 27 (2017) 1604604.
- [46] M. Wang, W. Wang, W.R. Leow, C. Wan, G. Chen, Y. Zeng, J. Yu, Y. Liu, P. Cai, H. Wang, D. Ielmini, X. Chen, Enhancing the matrix addressing of flexible sensory arrays by a highly nonlinear threshold switch, *Adv. Mater.* 30 (2018) 1802516.
- [47] Y. Shi, X. Liang, B. Yuan, V. Chen, H. Li, F. Hui, Z. Yu, F. Yuan, E. Pop, H.S. P. Wong, M. Lanza, Electronic synapses made of layered two-dimensional materials, *Nat. Electron.* 1 (2018) 458–465.
- [48] R. Wang, H. Li, L. Zhang, Y.-J. Zeng, Z. Lv, J.-Q. Yang, J.-Y. Mao, Z. Wang, Y. Zhou, S.-T. Han, Graphitic carbon nitride nanosheets for solution processed non-volatile memory devices, *J. Mater. Chem. C* 7 (2019) 10203–10210.
- [49] G. Wang, J.-H. Lee, Y. Yang, G. Ruan, N.D.-Kim, Y. Ji, J.M. Tour, Three-dimensional networked nanoporous Ta₂O₅-x memory system for ultrahigh density storage, *Nano Lett.* 15 (2015) 6009–6014.
- [50] M. Wang, S. Cai, C. Pan, C. Wang, X. Lian, Y. Zhuo, K. Xu, T. Cao, X. Pan, B. Wang, S.-J. Liang, J.J. Yang, P. Wang, F. Miao, Robust memristors based on layered two-dimensional materials, *Nat. Electron.* 1 (2018) 130–136.
- [51] B. Hwang, J.S. Lee, Lead-free, air-stable hybrid organic-inorganic perovskite resistive switching memory with ultrafast switching and multilevel data storage, *Nanoscale* 10 (2018) 8578–8584.
- [52] H. Wang, Y. Du, Y. Li, B. Zhu, W.R. Leow, Y. Li, J. Pan, T. Wu, X. Chen, Configurable resistive switching between memory and threshold characteristics for protein-based devices, *Adv. Funct. Mater.* 25 (2015) 3825–3831.
- [53] J. Yoo, J. Woo, J. Song, H. Hwang, Threshold switching behavior of Ag-Si based selector device and hydrogen doping effect on its characteristics, *AIP Adv.* 5 (2015) 127221.
- [54] Y. Yang, J. Lee, S. Lee, C.H. Liu, Z. Zhong, W. Lu, Oxide resistive memory with functionalized graphene as built-in selector element, *Adv. Mater.* 26 (2014) 3693–3699.
- [55] W. Xue, G. Liu, Z. Zhong, Y. Dai, J. Shang, Y. Liu, H. Yang, X. Yi, H. Tan, L. Pan, S. Gao, J. Ding, X.-H. Xu, R.-W. Li, A 1D vanadium dioxide nanochannel constructed via electric-field-induced ion transport and its superior metal-insulator transition, *Adv. Mater.* 29 (2017) 1702162.
- [56] Q.-D. Ling, Y. Song, S.-L. Lim, E.-Y.-H. Teo, Y.-P. Tan, C. Zhu, D.S.H. Chan, D.-L. Kwong, E.-T. Kang, K.-G. Neoh, A dynamic random access memory based on a conjugated copolymer containing electron-donor and -acceptor moieties, *Angew. Chem. Int. Ed.* 118 (2006) 3013–3017.
- [57] J. Bae, I. Hwang, Y. Jeong, S.-O. Kang, S. Hong, J. Son, J. Choi, J. Kim, J. Park, M.-J. Seong, Q. Jia, B. Ho Park, Coexistence of bi-stable memory and mono-stable threshold resistance switching phenomena in amorphous NbOx films, *Appl. Phys. Lett.* 100 (2012), 062902.
- [58] J. Ho Lee, G. Hwan Kim, Y. Bae Ahn, J. Woon Park, S. Wook Ryu, C. Seong Hwang, H. Joon Kim, Threshold switching in Si-As-Te thin film for the selector device of crossbar resistive memory, *Appl. Phys. Lett.* 100 (2012) 123505.
- [59] J. Song, A. Prakash, D. Lee, J. Woo, E. Cha, S. Lee, H. Hwang, Bidirectional threshold switching in engineered multilayer (Cu₂O/Ag:Cu₂O/Cu₂O) stack for cross-point selector application, *Appl. Phys. Lett.* 107 (2015) 113504.
- [60] Q. Hua, H. Wu, B. Gao, M. Zhao, Y. Li, X. Li, X. Hou, M.F. Chang, P. Zhou, H. Qian, A threshold switching selector based on highly ordered Ag nanodots for X-point memory applications, *Adv. Sci.* 6 (2019) 1900024.
- [61] C. Zhang, J. Shang, W. Xue, H. Tan, L. Pan, X. Yang, S. Guo, J. Hao, G. Liu, R.W. Li, Convertible resistive switching characteristics between memory switching and threshold switching in a single ferritin-based memristor, *Chem. Commun.* 52 (2016) 4828–4831.
- [62] S. Jeonhwan, W. Jiyong, A. Prakash, L. Daeseok, H. Hyunsang, Threshold selector with high selectivity and steep slope for cross-point memory array, *IEEE Electron. Device Lett.* 36 (2015) 681–683.
- [63] J. Sung Hyun, T. Kumar, S. Narayanan, W.D. Lu, H. Nazarian, in: *IEEE International Electron Devices Meeting*, (San Francisco, CA, USA, 2014), 2014.
- [64] Q. Luo, X. Xu, H. Liu, H. Lv, T. Gong, S. Long, Q. Liu, H. Sun, W. Banerjee, L. Li, J. Gao, N. Lu, S.S. Chung, J. Li, M. Liu, in: *IEEE International Electron Devices Meeting (IEDM)*, (Washington, DC, USA, 2015), 2015.
- [65] Y.J. Baek, Q. Hu, J.W. Yoo, Y.J. Choi, C.J. Kang, H.H. Lee, S.H. Min, H.M. Kim, K. B. Kim, T.S. Yoon, Tunable threshold resistive switching characteristics of Pt-Fe₂O₃ core-shell nanoparticle assembly by space charge effect, *Nanoscale* 5 (2013) 772–779.
- [66] L. He, Z.M. Liao, H.C. Wu, X.X. Tian, D.S. Xu, G.L. Cross, G.S. Duesberg, I.V. Shvets, D.P. Yu, Memory and threshold resistance switching in Ni/NiO core-shell nanowires, *Nano Lett.* 11 (2011) 4601–4606.
- [67] M.J. Lee, D. Lee, S.H. Cho, J.H. Hur, S.M. Lee, D.H. Seo, D.S. Kim, M.S. Yang, S. Lee, E. Hwang, M.R. Uddin, H. Kim, U.I. Chung, Y. Park, I.K. Yoo, A plasma-treated chalcogenide switch device for stackable scalable 3D nanoscale memory, *Nat. Commun.* 4 (2013) 2629.
- [68] J. Park, T. Hadamek, A.B. Posadas, E. Cha, A.A. Demkov, H. Hwang, Multi-layered NiOy/NbOx/NiOy fast drift-free threshold switch with high Ion/Ioff ratio for selector application, *Sci. Rep.* 7 (2017) 4068.
- [69] H.Y. Peng, Y.F. Li, W.N. Lin, Y.Z. Wang, X.Y. Gao, T. Wu, Deterministic conversion between memory and threshold resistive switching via tuning the strong electron correlation, *Sci. Rep.* 2 (2012) 442.
- [70] J.-Y. Seo, J. Choi, H.-S. Kim, J. Kim, J.-M. Yang, C. Cuhadar, J.S. Han, S.-J. Kim, D. Lee, H.W. Jang, N.-G. Park, Wafer-scale reliable switching memory based on 2-dimensional layered organic-inorganic halide perovskite, *Nanoscale* 9 (2017) 15278–15285.
- [71] X. Guan, W. Hu, M.A. Haque, N. Wei, Z. Liu, A. Chen, T. Wu, Light-responsive ion-redistribution-induced resistive switching in hybrid perovskite Schottky junctions, *Adv. Funct. Mater.* 28 (2018) 1704665.
- [72] K. Qian, R.Y. Tay, V.C. Nguyen, J. Wang, G. Cai, T. Chen, E.H.T. Teo, P.S. Lee, Hexagonal boron nitride thin film for flexible resistive memory applications, *Adv. Funct. Mater.* 26 (2016) 2176–2184.
- [73] C. Gu, J.S. Lee, Flexible hybrid organic-inorganic perovskite memory, *ACS Nano* 10 (2016) 5413–5418.
- [74] J. Haruyama, K. Sodeyama, L. Han, Y. Tateyama, First-principles study of ion diffusion in perovskite solar cell sensitizers, *J. Am. Chem. Soc.* 137 (2015) 10048–10051.
- [75] A.M. Ritzmann, A.B. Muñoz-García, M. Pavone, J.A. Keith, E.A. Carter, Ab initio DFT+U analysis of oxygen vacancy formation and migration in La_{1-x}Sr_xFeO_{3-δ} (x=0, 0.25, 0.50), *Chem. Mater.* 25 (2013) 3011–3019.
- [76] Z. Zhang, Q. Ge, S.C. Li, B.D. Kay, J.M. White, Z. Dohnalek, Imaging intrinsic diffusion of bridge-bonded oxygen vacancies on TiO₂(110), *Phys. Rev. Lett.* 99 (2007) 126105.
- [77] S. Yu, X. Guan, H.S.P. Wong, Conduction mechanism of TiN/HfO₂/Pt resistive switching memory: a trap-assisted-tunneling model, *Appl. Phys. Lett.* 99 (2011), 063507.
- [78] Y. Yang, P. Gao, S. Gaba, T. Chang, X. Pan, W. Lu, Observation of conducting filament growth in nanoscale resistive memories, *Nat. Commun.* 3 (2012) 732.
- [79] J.Y. Mao, L. Zhou, X. Zhu, Y. Zhou, S.T. Han, Photonic memristor for future computing: a perspective, *Adv. Opt. Mater.* 7 (2019) 1900766.
- [80] Y.H. Liu, L.Q. Zhu, P. Feng, Y. Shi, Q. Wan, Freestanding artificial synapses based on laterally proton-coupled transistors on chitosan membranes, *Adv. Mater.* 27 (2015) 5599–5604.
- [81] W. Xu, H. Cho, Y.H. Kim, Y.T. Kim, C. Wolf, C.G. Park, T.W. Lee, Organometal halide perovskite artificial synapses, *Adv. Mater.* 28 (2016) 5916–5922.
- [82] E.S. Fortune, G.J. Rose, Short-term synaptic plasticity as a temporal filter, *Trends Neurosci.* 24 (2001) 381–385.
- [83] C. Du, W. Ma, T. Chang, P. Sheridan, W.D. Lu, Biorealistic implementation of synaptic functions with oxide memristors through internal ionic dynamics, *Adv. Funct. Mater.* 25 (2015) 4290–4299.
- [84] M. Kumar, H.S. Kim, J. Kim, A highly transparent artificial photonic nociceptor, *Adv. Mater.* 31 (2019) 1900021.
- [85] B. Li, Y. Liu, C. Wan, Z. Liu, M. Wang, D. Qi, J. Yu, P. Cai, M. Xiao, Y. Zeng, X. Chen, Mediating short-term plasticity in an artificial memristive synapse by the orientation of silica mesopores, *Adv. Mater.* 30 (2018) 1706395.
- [86] L. Hu, S. Fu, Y. Chen, H. Cao, L. Liang, H. Zhang, J. Gao, J. Wang, F. Zhuge, Ultrasensitive memristive synapses based on lightly oxidized sulfide films, *Adv. Mater.* 29 (2017) 1606927.
- [87] Z. Wang, S. Joshi, S.E. Savel'ev, H. Jiang, R. Midya, P. Lin, M. Hu, N. Ge, J. P. Strachan, Z. Li, Q. Wu, M. Barnell, G.L. Li, H.L. Xin, R.S. Williams, Q. Xia, J. Yang, Memristors with diffusive dynamics as synaptic emulators for neuromorphic computing, *Nat. Mater.* 16 (2017) 101–108.

- [88] J.-Y. Mao, L. Zhou, Y. Ren, J.-Q. Yang, C.-L. Chang, H.-C. Lin, H.-H. Chou, S.-R. Zhang, Y. Zhou, S.-T. Han, A bio-inspired electronic synapse using solution processable organic small molecule, *J. Mater. Chem. C* 7 (2019) 1491–1501.
- [89] Y.-N. Zhong, T. Wang, X. Gao, J.-L. Xu, S.-D. Wang, Synapse-like organic thin film memristors, *Adv. Funct. Mater.* 28 (2018) 1800854.
- [90] S. Choi, J. Lee, S. Kim, W.D. Lu, Retention failure analysis of metal-oxide based resistive memory, *Appl. Phys. Lett.* 105 (2014) 113510.
- [91] C. Chen, S. Gao, F. Zeng, G.S. Tang, S.Z. Li, C. Song, H.D. Fu, F. Pan, Migration of interfacial oxygen ions modulated resistive switching in oxide-based memory devices, *J. Appl. Phys.* 114 (2013), 014502.
- [92] H. Tian, Q. Guo, Y. Xie, H. Zhao, C. Li, J.J. Cha, F. Xia, H. Wang, Anisotropic black phosphorus synaptic device for neuromorphic applications, *Adv. Mater.* 28 (2016) 4991–4997.
- [93] J.-Y. Mao, L. Hu, S.-R. Zhang, Y. Ren, J.-Q. Yang, L. Zhou, Y.-J. Zeng, Y. Zhou, S.-T. Han, Artificial synapses emulated through a light mediated organic–inorganic hybrid transistor, *J. Mater. Chem. C* 7 (2019) 48–59.
- [94] Y. Yuan, J. Chae, Y. Shao, Q. Wang, Z. Xiao, A. Centrone, J. Huang, Photovoltaic switching mechanism in lateral structure hybrid perovskite solar cells, *Adv. Energy Mater.* 5 (2015) 1500615.
- [95] R.A. John, N. Yantara, Y.F. Ng, G. Narasimman, E. Mosconi, D. Meggiolaro, M. R. Kulkarni, P.K. Gopalakrishnan, C.A. Nguyen, F. De Angelis, S.G. Mhaisalkar, A. Basu, N. Mathews, Ionotronic halide perovskite drift-diffusive synapses for low-power neuromorphic computation, *Adv. Mater.* 30 (2018) 1805454.